Microchemical evidence for episodic growth of antitaxial veins during fracture-controlled fluid flow

Shaun L.L. Barker [a,*] Stephen F. Cox [a,b] Stephen M. Eggins [a] Michael K. Gagan [a]

[a] *Research School of Earth Sciences, The Australian National University, Canberra, ACT 0200, Australia*

[b] *Department of Earth and Marine Sciences, The Australian National University, Canberra, ACT 0200, Australia*

.

Abstract

The mechanism by which syntectonic hydrothermal veins form is widely debated, with some workers suggesting that certain vein textures are related to specific fluid flow regimes. Central to the debate is whether vein formation involves advective fluid flow, or occurs by local diffusion of material from the surrounding wall rock. To address this issue, we integrated textural observations and microchemical analyses of a hydrothermal vein from the Lachlan Orogen, southeast Australia, to reveal information about vein growth history, changes in fluid chemistry, and the evolution of fluid flow pathways during vein growth. The study area is part of a regional-scale fault-fracture network in an interbedded limestone-shale sequence, which formed at depths of ∼5–10 km (∼150–200°C) during late Devonian crustal shortening. This integrated approach demonstrates that the zonation of textures, Sr isotopes, stable isotopes (C,O), and trace and rare earth elements is distinctly asymmetrical about the median growth-line of the vein. δ^{18}O values in vein calcite (17.0–18.8 ‰, VSMOW) are lower than those in surrounding unaltered limestones (23–25 ‰, VSMOW), and vary systematically across the vein. In contrast, δ^{13}C values are relatively constant across most of the vein, but become markedly depleted (*ca.* 4 ‰) immediately adjacent to the wall rock. This strong depletion in δ^{13}C was probably caused by the influx of more oxidised fluids during the latest stages of vein growth. Strontium isotope ratios (^{87}Sr/^{86}Sr) vary between 0.70912 and 0.70931 across the vein. Abrubt changes in ^{87}Sr/^{86}Sr, δ^{18}O, Ce/Ce*, Eu/Eu* and trace element concentrations indicate that vein growth was accompanied by stepwise changes in the fluid flow pathway and consequent variations in fluid chemistry. Taken together, our findings are not consistent with growth of fibrous antitaxial veins by diffusional transfer of material from the surrounding wallrock. Instead, they suggest that externally sourced fluids migrated along episodically changing fracture-controlled flow

pathways. This has implications for the dynamics of crustal permeability and mineralisation.

Key words: vein, calcite, strontium isotopes, fluid flow, carbon and oxygen isotopes, rare earth elements

1 Introduction

Veins in rocks have been studied for well over 150 years, initially driven by interest in how economically mineralised veins formed (e.g. 1; 2). Veins provide information on how fluids migrate through the crust, and how material is transferred by these fluids.

Many studies have suggested that veins (including 'crack-seal' textured veins; 3) form as a result of brittle failure, fracture dilation, fluid infiltration and subsequent mineral precipitation (e.g. 3; 4; 5; 6; 7). However, some recent studies have also suggested that vein formation can occur without fracture, with vein growth driven by diffusional transport of material from the immediately surrounding rock mass (8; 9).

The mechanism by which veins form has been increasingly debated over recent years, with argument centered over the necessity for void formation prior to vein growth, and whether veins record advective or diffusive mass transfer in the crust. Different vein textures (e.g. fibrous, elongate blocky, crack-seal, stretched crystal, blocky) form as vein opening and crystal growth kinetics vary (3; 4; 6; 7; 10; 11). Some previous workers have suggested that certain vein textures (e.g. fibrous textures) are related to diffusional mass transfer, while other textures (e.g. blocky) are related to advective flow regimes (10; 12).

Fibrous veins are of particular interest, as they provide a record of progressive displacement paths during vein opening (13). Regularly oriented and spaced inclusion bands across mineral fibres are interpreted to indicate that fibrous to elongate blocky vein textures develop via a crack-seal mechanism (3).

Transport of material via fluid occurs by two main mechanisms (12):

(1) *Diffusional transport* is driven by chemical potential gradients, with ma-

* Corresponding author.
Email addresses: shaun.barker@anu.edu.au (Shaun L.L. Barker), stephen.cox@anu.edu.au (Stephen F. Cox), stephen.eggins@anu.edu.au (Stephen M. Eggins), michael.gagan@anu.edu.au (Michael K. Gagan).

terial moving through a fluid, which may be stationary or migrating. Diffusion through a fluid is relatively slow, and is most effective over distances of centimetres to decimetres in non-advecting fluid regimes (14).

(2) During *advective transport* material is carried in a migrating fluid. This can occur throughout a permeable rock mass, or within discrete fractures. Advective fluid flow may occur over large distances, and is a very effective material transport mechanism. It has been suggested that elongate-blocky, blocky and crack-seal textures develop in advective flow regimes (10; 12).

Recently, it has been suggested that veins (perhaps even 'crack-seal' textured veins) may form without fracture, as a result of growing crystals forcing the wall rock apart in a diffusional mass transfer regime (8; 9). In addition, two experimental vein growth studies concluded that lateral advection of fluid through fractures and accompanying precipitation of material can lead to inlet clogging and cessation of flow (15; 16). These studies call into question the influence of veins (particularly extension veins) on crustal permeability.

In this contribution, we highlight the importance of integrated microstructural observations and microchemical analyses to examine the growth history and fluid chemistry changes accompanying the formation of a syntectonic vein. Suites of elements and isotopes are used to differentiate variations in fluid chemistry. These changes are interpreted in terms of variable fluid reservoir chemistry, and the effects of fluid-rock reaction along flow pathways. To the best of our knowledge, this is the first study of syntectonic veins to utilise high-spatial resolution (100 μm) analyses of C, O and Sr isotopes and trace element concentrations. These high-spatial resolution chemical analyses will be used to show that fluid pathways and/or fluids sources change in a stepwise manner during the growth of a single antitaxial fibrous vein.

2 Geological setting and sample description

The antitaxial fibrous vein described occurs within an interbedded limestone-shale sequence, the Cavan Bluff Limestone. This limestone forms part of the Murrumbidgee Group (17; 18) in the Eastern Belt of the Lachlan Orogen, in eastern New South Wales, Australia (19). The Murrumbidgee Group is composed of several formations, comprising massive grey micritic limestones, redbed sandstones and shales, and thinly interbedded (10–20 cm scale) limestones and shales. The sedimentary sequence has been folded into a series of upright, open to close folds, and was probably deformed during mid-late Devonian crustal shortening (17). Oxygen isotope quartz-calcite thermometry (Cox, unpublished data) suggests that veins formed at temperatures of 150–200° C. The depth of vein formation may have been between 5 and 10 km. An

extensive fault-fracture network is developed over an area of approximately 20 km^2. Folding and veining were synchronous, with a variety of fault veins, bedding-parallel slip veins and extension veins developed. A stable C and O isotope study by Cox (unpublished data) indicates that veins formed from externally derived, upward migrating fluids of probable meteoric origin (initial low δ^{18}O fluids).

This paper focuses exclusively on the internal structure and chemistry of a subvertical bedding-parallel extension vein, which is approximately $\sim$ 1–1.5 cm thick, and at least 5 m long. The vein occurs around 20 m east of a larger (*ca.* 150 m long), subvertical, calcite-mineralised fault zone, and associated fault-fracture network. This vein is an early formed member of the regionally extensive vein network. The vein lies about 30 m structurally above the base of the Murrumbidgee Group. The vein is composed of calcite, with rare barite fibres also present. It has an asymmetric fibrous texture, with fibres increasing in width from a median line which is present approximately two-thirds of the distance across the vein (Fig. 1). Some fibres extend from the median line to wall rock (8–10 mm), with widths increasing from approximately 5–10 μm at the median line to $\sim 250 - 300$ μm near the vein margin.

Five distinct textural zones (TZ) are evident in hand specimen and thin section. These zones are parallel to the vein walls (Fig. 1), and are characterised by variations in calcite colour, cathodoluminescence and/or fibre orientation and thickness. Textural zone 1 comprises a very thin zone ($\sim$150–200 μm) immediately adjacent to the wall rock, and has the brightest colour in cathodoluminesence (CL). Textural zone 2 is 0.5–1 mm thick, and has the lowest CL intensity. Textural zone 3 is 2 mm thick, has moderate CL intensity, and fibres have a slightly different orientation ($\sim 5^\circ$) to those in TZ 2. Textural zone 4 is 5 mm thick, and together with TZ 5 (5 mm thick) forms the oldest part of the vein. TZ 4 and 5 have asymmetric microstructures, with TZ 5 developing thicker fibres than TZ 4.

This vein matches the strict definition for fibrous veins outlined in (10), and has an antitaxial growth morphology, with the oldest material at the median line, and the youngest material at the vein margin (10; 12; 13). Polished thick and thin sections were made perpendicular to bedding, and parallel to the fibre long axes. Trace element and isotopic analyses were conducted on the immediately adjacent polished thick section from which the thin section was cut (illustrated in Figure 1).

3 Analytical Methods

3.1 Trace Element Analyses

The spatial distribution of selected minor and trace elements (Si, Mg, Fe, Sr) was investigated by production of electron microprobe maps conducted on a Cameca SX100. A defocused 10 μm beam, set at 15 kV and 100 nA was used. Counts were collected for 200 ms per point, with 20 μm between adjacent points.

Distributions of trace elements were measured in situ by laser-ablation inductively coupled plasma mass spectrometry (LA-ICP-MS). Samples were analysed using a pulsed ArF Excimer laser (λ=193 nm) and a quadrupole ICP-MS (Agilent 7500s). The sample was moved at a steady speed ($\sim$ 30 μm s^{-1}) beneath the laser beam, facilitating in situ, high spatial resolution, continuous data collection (20). Samples were precleaned with ethanol, and the area chosen for analysis was 'laser cleaned' by a laser ablation pre-scan. Sampling was carried out approximately parallel to the long axes of fibres. Two traverses were carried out across the vein, separated by approximately 5 mm. In addition, a single fibre was analysed from TZ 1 to the median line.

Multiple major and trace elements (^{23}Na,^{24}Mg, ^{29}Si, ^{43}Ca, ^{44}Ca, ^{45}Sc, ^{49}Mn, ^{57}Fe, ^{85}Rb, ^{88}Sr, ^{89}Y, ^{138}Ba, ^{139}La, ^{140}Ce, ^{141}Pr, ^{146}Nd, ^{147}Sm, ^{153}Eu, ^{158}Gd, ^{163}Dy, ^{166}Er, ^{174}Yb, ^{208}Pb, ^{232}Th, ^{238}U) were simultaneously profiled during laser sampling by repeated, rapid sequential peak hopping, with a mass spectrometer cycle time of 0.65 s. Data reduction followed established protocols for time-resolved analysis (21). High spatial resolution was achieved by using 20 μm spots at 20 laser pulses per second with a moderately low laser fluence (5 J cm^{-2}), and by minimising mean particulate residence times in the ablation cell volume following each laser pulse. Data is binned over 1 second intervals, giving a spatial resolution of 30 μm. Internal standardisation is carried out using ^{43}Ca.

3.2 Strontium isotope analyses

Sr isotope compositions were analysed in situ by laser ablation multi-collector inductively coupled plasma mass spectrometry (LA-MC-ICPMS). Analyses were carried out at the Australian National University, using a HelEx ArF excimer laser ablation system, interfaced to a Finnigan MAT Neptune MC-ICPMS (see 20; 22, for details). Details of the large sample holding and high spatial resolution analytical capabilities of this instrumentation are documented in (22). For the purposes of this study, analyses have been performed

using a spot approach (137–233 μm size). Laser pulse rates of 5 Hz in combination with a laser fluence of 5 J/cm^2 , short laser wavelength (λ= 193 nm), and aperture imaging optics were used to attain controlled calcite ablation ($\sim$1 μm per second) in a He ablation medium (20).

The Finnigan MAT Neptune MC-ICPMS is equipped with a moveable array of 9 Faraday cups that were located to monitor all Sr isotopes and peak-strip key interfering species (Kr, Rb and REE^{++}). Faraday cups were positioned to the high mass-side of peak-centres to minimize potential REE^{++} overlaps following the approach of (see Table 1 23). The Finnigan Neptunes gas flow and electrostatic lens settings were optimised for maximum Sr sensitivity and peak-shape while ablating a modern Tridachna clam shell which has a measured ^{87}Sr/^{86}Sr value of 0.709143$\pm$15 (24). Tridachna was additionally used to monitor instrument reproducibility and accuracy. For 22 analyses of Tridachna, the average ^{87}Sr/^{86}Sr ratio was 0.709149 $\pm$38 (2σ) All data were obtained using 1.024 s integration periods, for total analysis times of 200 seconds. Data reduction involved subtraction of on-peak baselines, measured every 20-30 minutes (every 5-6 spot analyses), from raw peak intensities. This was followed by correction of instrumental mass fractionation using an exponential law based on the measured ^{86}Sr/^{88}Sr ratio and a canonical value of 0.1194. Removal of any ^{87}Rb contribution to measured ^{87}Sr was undertaken using the measured ^{85}Rb and mass fractionation factor measured for Sr. Krypton interference was accounted for via stripping of on-peak baselines. REE^{++} interferences were found to be negligible in all measurements.

3.3 Stable isotope analyses

Samples for stable isotope analysis were collected across the vein, parallel to fibre long axes. An automated milling machine was used to sequentially remove samples over 100 μm intervals (with a total volume of 1.6 x 4 x 0.1 mm collected for each sample), yielding approximately 2 mg of calcite (25). High-pressure air was used to remove calcite dust from the mill between each sample to prevent cross contamination.

Oxygen and carbon isotope ratios were measured on a Finnigan MAT 251 mass spectrometer. For each sample, 200 ± 20 μg of powder was dissolved in 103% H_3PO_4 at 90° in an automated carbonate (Kiel) device. Carbon isotope ratios are reported relative to Vienna Peedee Belemnite (VPDB). O isotope results are reported relative to VSMOW, and were converted from VPDB values, where $\delta^{18}O_{VSMOW}$=1.03091$\delta^{18}O_{VPDB}$ + 30.91 (26).

Isotope results have been normalised on the VSMOW and VPDB scales so that analyses of:

NBS-19 $\delta^{18}O_{VPDB}$ = -2.20 ‰; $\delta^{18}O_{SMOW}$ = + 28.64 ‰ and $\delta^{13}C_{VPDB}$ = +1.95 ‰
NBS-18 $\delta^{18}O_{VPDB}$ = -23.0 ‰; $\delta^{18}O_{SMOW}$ = + 7.2 ‰ and $\delta^{13}C_{VPDB}$ = +5.0 ‰

The standard deviation (2σ) for the 19 replicate standards used during the analysis of these samples was 0.02 ‰ for $\delta^{13}C$ and 0.07 ‰ for $\delta^{18}O$.

4 Results

In the following section, results from the various chemical analyses are described. Variations on all scales are considered; fine scale ($< 0.1 - 0.5$ mm), textural zone scale (0.5–5 mm) and over the whole vein. Potential causes for chemical variation are discussed in section 5.

4.1 Isotopes

The measured $^{87}Sr/^{86}Sr$ ratios (and associated analytical errors) across the vein are shown in Figure 2. Strontium isotope ratios change significantly across the vein, with $^{87}Sr/^{86}Sr$ ratios highest in TZ 2, and lowest in TZ 3. The most significant change is observed between textural zones 2–4, with TZ 4 and 5 being indistinguishable (Table 2, Fig. 2). The $^{87}Sr/^{86}Sr$ ratio varies between 0.70812 and 0.70831. Textural zones 2 (average $^{87}Sr/^{86}Sr$=0.70829), 3 (average $^{87}Sr/^{86}Sr$=0.70815) and 4 (average $^{87}Sr/^{86}Sr$=0.70823) have Sr isotope ratios which are significantly different at the 2σ confidence level (Fig. 2).

$\delta^{18}O$ and $\delta^{13}C$ values in vein calcite vary systematically with distance through the vein (Figure 3). $\delta^{18}O$ values range between 17.0 ‰ and 18.8 ‰. The $\delta^{18}O$ values are lower than those in the proximal host limestones, which are typically 19–21 ‰. In comparison, $\delta^{18}O$ in the distal limestones (more than 50 m from a major fault zone) is ∼23–25 ‰. In TZs 4 and 5, oxygen isotope ratios are most depleted immediately adjacent to the median line, and generally increase with decreasing age toward the vein margins. Notably, the oxygen isotope profiles on either side of the median line are distinctly asymmetric. With decreasing age in TZ 5, $\delta^{18}O$ values become less depleted than at an equivalent distance from the median line in TZ 4. At the transition between TZs 3 and 4, $\delta^{18}O$ decreases from $\sim$ 17.5 ‰ to 17 ‰. Oxygen isotope values reach their lowest point at the boundary between TZ 2 and 3, and increase toward the vein wall-rock boundary from 17 ‰ to 18.2 ‰ within TZ 1. Within each textural zone (particularly zones 4 and 5), oxygen isotope ratio changes are not monotonic, and positive and negative excursions of $\pm$ 0.3–0.4 ‰ from the general trend occur over distances of < 0.5 mm. The sampling method leads to smoothing of isotopic ratios due to the coarse sampling size employed.

δ^{13}C values vary between -4.46 ‰ and 1.63 ‰. Carbon isotope values are similar throughout textural zones 4 and 5, with a slight decrease (about 0.5 ‰) with decreasing age from the median line in textural zone 5. There is no comparable decrease with distance from the median line in TZ 4. In textural zone 3, δ^{13}C values generally decrease with decreasing age toward the vein-wall rock interface, from values of *ca.* 1 ‰ to -4 ‰, although there are departures from this trend in TZ 2 and near the boundary of TZ 3 and TZ 2. In comparison, the host limestones δ^{13}C are between -1 and +3 ‰.

4.2 Trace elements

Trace element uptake by calcite varies as a function of precipitation rate, temperature, solution chemistry, crystal morphology and crystal growth rate (see 27; 28). Here, variations in selected trace and REEs are outlined. These results are further discussed and interpreted in section 5.2. Electron microprobe maps and LA-ICP-MS analyses showing the distribution of Sr, Fe and Mg across the vein at two different locations (separated by 5 mm) are shown in Figure 4a. In the grey scale EMP maps, lighter colours represent areas of higher concentration. The wallrock-vein boundary is marked by a transition from high Si to low Si concentrations (see supplementary data set). The major textural zones can be distinguished by the concentrations of Fe and Sr. Strontium concentrations are highest in TZ 1, lowest in TZ 2, and are then relatively homogeneous excepting high spatial-frequency oscillations throughout the rest of the vein. An apparently late, crosscutting band of high Sr calcite occurs within TZ 5 (point 'α' in Figure 4). Fe concentrations decrease with decreasing age in TZ 4 and 5, and drop markedly in TZ 3. In TZ 3 and 4, some adjacent fibres, which are interpreted to have grown at the same time (according to the current understanding of fibrous vein growth), have distinctly different concentrations of Mg, Fe and Sr (Fig. 4a). Iron, Sr and Sc concentration changes can be correlated well between traverses, while Mg shows significant differences.

Concentration data for additional elements can be found in the supplementary data set. Key features indicated by the line profiles are:

(1) Significant fluctuations (up to several thousand ppm) are shown by all elements on scales of < 1 mm.
(2) TZ 1 has higher concentrations of Sr, Mg, Y, Sc, and the HREE (Fig. 6) than the other textural zones.
(3) TZ 3 has generally lower concentrations of Fe than other parts of the vein.
(4) Within TZ 4 and 5, the highest concentrations of Yb, Sc and HREEs occur immediately adjacent to the median line.
(5) Trace and REE concentration profiles are generally asymmetric about

the median line in TZ 4 and 5.

An analysis of a single fibre extending across TZ 1 to 4 shows similar variations for Fe and Sr as observed for the traverse carried across the vein (which sampled several fibres; Fig. 4b). Trace and REE concentrations vary significantly along this single fibre (see supplementary data set).

Trace and rare earth concentrations vary on all scales. On the finest scale (between adjacent data points; 30 μm) Fe concentrations typically change by between 5 and 50 %. Over larger distances (0.2–0.5 mm), there are systematic changes in the concentrations of all minor and trace elements analysed. For example, Fe concentrations change by more than 1000 ppm with decreasing age in TZ 4. Rubidium has concentrations at or near detection limits ($<$ 0.5 ppm) throughout the calcite vein. Yttrium, Sc and the heavy REEs (Yb and Lu), show similar behaviour across the vein, with highest concentrations immediately adjacent to the median line and in TZ 1. The REE concentrations reported here are similar to those reported for calcite in filled fractures by (29).

The REEs can provide information on fluid chemistry (e.g. complexing species) and oxidation state (30). Graphs of Ce/Ce* and Eu/Eu* (where Ce* and Eu* are the values predicted from the adjacent normalised REEs; 31) are presented in Figure 5. Ce/Ce* values have an average value of 1.05–1.1 throughout much of the vein. Eu/Eu* values are more variable, with changes of up to 0.5 from an average value of $\sim$ 1.1. However, in TZs 1–3, Eu/Eu* values change markedly, and reach their lowest values (*ca.* 0.6). Over the same region of the vein, Ce/Ce* values increase to 1.3. Generally, Ce/Ce* and Eu/Eu* ratios are covariant, with an opposite sense of variation (i.e. an increase in Eu/Eu* is accompanied by a decrease in Ce/Ce*).

In addition to information on oxidation state, normalised REE patterns in calcite may provide information on changes in REE complexation in the parent solution, particularly changes in $[CO_3^{2-}]$ (see section 5.2, Fig 6a). Rare earth element concentrations were normalised to chondrite (32). The slope and regression coefficient of REE patterns (atomic number plotted against normalised REE value) was calculated by linear regression at 30 μm intervals (in the same manner as other elemental concentrations). All slopes are negative (indicating relative LREE enrichment) and generally linear (average r^2=0.86). The spatial distribution of slopes across the vein is presented in Figure 6b. Over small distances ($<$ 0.5 mm) slopes are highly variable, in a similar manner to the trace element concentrations. The distribution of REE slopes about the median line is distinctly asymmetric. In TZ 3, slopes decrease, indicating relative enrichment in the HREE. Textural zones 1 and 2 are distinctly enriched in the HREE, Y and Sc.

5 Discussion

In the following section we integrate the textural and chemical information presented above. By integrating textural and chemical data, inferences can be made about fluid chemistry and the role of fluid-rock reactions along fluid pathways during the growth of an individual vein.

5.1 Isotope signatures - fluid source and fluid pathways

Generally, Sr isotopes are believed not to undergo any significant mass fractionation during most geological processes (33). Hence, the Sr isotope signature of a fluid will reflect the Sr isotope values of the rocks with which that fluid has equilibrated, and the extent of isotopic exchange along the flow pathway. In this vein, which has very little Rb (< 0.5 ppm) compared to Sr, the $^{87}Sr/^{86}Sr$ variations will reflect changes in the Sr isotope signature of the fluid from which that vein formed, rather than any effects of ^{87}Rb radioactive decay. Strontium isotopes can be used to provide insights about the chemistry of the fluid source and/or isotopic exchange along fluid pathways during vein formation. If fluids come from the same fluid source, and have the same degree of fluid-rock reaction (i.e. same fluid flow pathway and flow rate), then they would be expected to precipitate calcite with identical Sr isotope ratios.

In this vein, $^{87}Sr/^{86}Sr$ ratios vary between 0.70812 and 0.70831 (Fig. 2b). Two analyses of the carbonate component of Cavan Bluff Limestone collected at a distance from major fault zones have $^{87}Sr/^{86}Sr$ of 0.70828 ± 0.03 (Barker et al, unpublished data). These values are within the range of values for Devonian seawater (34). Critically, it is the small differences in $^{87}Sr/^{86}Sr$ *within* the vein that reveal how fluid source compositions and/or fluid-rock reaction (and hence fluid pathways) may have varied as the vein grew.

The Sr isotope analyses indicate that small but significant $^{87}Sr/^{86}Sr$ changes occur across TZ 1–4. As the vein grew, $^{87}Sr/^{86}Sr$ ratios became lower in TZ 3 and higher in TZ 2 (Fig. 7). These changes indicate that either the fluid pathways or the fluid source changed as the vein grew. The fluctuating $^{87}Sr/^{86}Sr$ values suggest that each stage of vein growth (marked by the different textural zones) occurred from a fluid that had reacted with rocks with different Sr isotope compositions (Fig. 7). This implies that fracture-controlled flow paths (or the chemistry of fluid reservoirs) changed dynamically with time. The study of Elburg et al (2002) (35) examined the Sr isotope and trace element compositions of antitaxial fibrous veins in South Australia. Figure 2g of their study documents $^{87}Sr/^{86}Sr$ variations through different regions of a fibrous vein. This figure clearly demonstrates that the $^{87}Sr/^{86}Sr$ signatures change as

calcite fibres grow. The data of (35) demonstrates that the intravein Sr isotope variations documented in this study are not isolated to a particular location, and may be a common phenomenon.

The δ^{18}O values of the vein are more depleted than the surrounding host rocks. This indicates that the fluid from which the vein formed was out of equilibrium with the host rocks, and was externally derived. In addition, the asymmetry in the evolution of δ^{18}O and δ^{13}C on either side of the median line implies a variation in vein growth rate, or asynchronous growth of TZs 4 and 5. In textural zones 1, 2, 4 and 5, $\delta^{18}O$ values become closer to wall-rock values with decreasing age. The progressively increasing δ^{18}O values could be explained by a temperature decrease during calcite growth. A temperature decrease of approximately 15–20 °C during the growth of TZ 5 would be sufficient to explain the change in δ^{18}O (36). If the increase in $\delta^{18}O$ was due to decreasing temperature, then a slight *positive* increase in $\delta^{13}C$ (approximately 0.06 ‰) would also be anticipated (37). Instead, $\delta^{13}C$ decreases by approximately 0.5 ‰.

We suggest that an initially isotopically depleted fluid entered the vein site, and began precipitating calcite at the median line. Progressively increasing δ^{18}O with time indicates that the fluid δ^{18}O became progressively more rock-buffered with time. This could be caused by an increase in reactive path length, or a decrease in fluid flow rate (causing enhanced fluid-rock reaction).

5.2 Trace element chemistry

One key result of our high-spatial resolution trace element analyses are the significant fine-scale (sub-millimetre) variations observed parallel to vein fibres. If these changes reflect fluctuations in bulk fluid chemistry then this would have significant implications, perhaps reflecting some cyclic variation in crustal permeability during vein growth. In this section, the possible causes for the fine-scale changes, in addition to the broader-scale changes are discussed. We also explain how the REEs may provide information on changes in fluid chemistry during vein growth.

The traverse along a single fibre (Fig. 4b) indicates that the fine-scale variations occur along individual fibres, and are not a sampling artifact caused by multiple fibres being crossed during laser ablation traverses. The fine-scale trace element variations could be caused by some form of supersaturation-nucleation-depletion (SND) disequilibrium cycle. These are explained in detail by (38). Briefly, precipitation of a mineral leads to consumption of elements which form that mineral. This prevents precipitation of that mineral in adjacent areas. This leads to fine-scale chemical variability, even from fluids in

equilibrium with the precipitating mineral. The influence of SND cycles on trace element incorporation in calcite could be tested by experimental growth of calcite crystals. Such an experiment is beyond the scope of this paper. It is important to note that neither crystal-growth controls nor SND cycles will affect the Sr isotope compositions of vein calcite (33).

The enrichment of heavy REEs observed in TZ 1 (Fig. 6) is accompanied by increased concentrations of Mg, Fe and Sr, more rock-buffered O isotope compositions, and lighter C isotope compositions (Fig. 3). These changes are probably due to the influx of a fluid with a chemical composition distinct from the fluids from which TZs 2–5 formed. The trace elements support the Sr and O isotope evidence, which suggests that the vein formed from fluids whose chemistry varied distinctly with time. These chemical variations could potentially arise from chemical changes in fluid reservoirs, or from the variable nature of fluid-rock interaction along changing flow paths.

In hydrothermal fluids, REE fractionation is a function of (a) sorption and desorption of REEs during migration of REE-bearing fluids along particle surfaces, and (b) coprecipitation (30). Carbonate and OH^- ligands form stronger complexes with HREEs than LREEs. In carbonate-dominated hydrothermal solutions (such as those which would be expected in limestones), low CO_3^{2-} concentrations will have flatter chondrite normalised REE patterns than solutions rich in CO_3^{2-} (see Figure 6a, 30). This is because in CO_3^{2-} poor solutions there will be little difference in the complexing of the light and heavy REEs. Figure 6 shows the variation in REE normalised patterns with distance across the vein, and illustrates which parts of the vein are relatively enriched in the light or heavy REEs. Notable in this graph are the high frequency oscillations in slope over short distances. These oscillations are similar to those previously noted for trace elements, and may be caused by changes in bulk fluid chemistry, or the SND cycles discussed above. Relative enrichment or depletion of CO_3^{2-} during vein growth could cause changes in the absolute concentration, and relative enrichment of light or heavy REEs in calcite. There is the potential to use REEs to trace changes in carbonate concentrations in fluids from which fault and vein-filling calcite precipitated. Further experimental work is needed to explore this.

5.3 Fluid oxidation

In TZ 1–3, $\delta^{13}C$ signatures become depleted (up to 5 ‰) compared to the $\delta^{13}C$ in the rest of the vein. One mechanism to create depleted $\delta^{13}C$ values is by fluid oxidation. Organic matter (e.g. CH_4) is heavily depleted in the heavier ^{13}C isotope. At low temperatures, isotopic equilibration between CO_2 and CH_4 (and other organic species) is very slow (estimated at 10^{10} years

at 200°C; 39). Hence, the organic carbon species must be oxidised so that the isotopically light carbon can be incorporated into carbonate. One simple oxidation mechanism is :

$$RCH_2O + FeOOH + 8H^+ = 4Fe^{2+} + CO_2 + 7H_2O + R \quad (1)$$

where R refers to organic matter which did not react (39).

The depleted $\delta^{13}C$ signatures found in TZ 1–3 record the influx of fluids containing ^{13}C depleted species which have been oxidised. This oxidation could have occurred in red bed sandstones, which occur stratigraphically above and below the Cavan Bluff Limestone.

Further evidence for changes in the degree of fluid oxidation during vein growth is shown by the Ce/Ce* ratios (Fig. 5). Cerium occurs as both a trivalent and tetravalent ion, depending on its oxidation state. In a fluid where all the Ce occurs in the 3^+ valency, with initially chondritic REE ratios, then Ce_{CN} should fall on the same trend in a normalised REE pattern as its immediate neighbours (La_{CN} and Pr_{CN}). However, if some Ce becomes oxidised into the 4^+ valency, it is possible that a Ce anomaly may occur in calcite precipitated from that fluid.

Eu anomalies are likely controlled by the Eu content of the host rocks with which fluids are reacting, as well as the oxidation state of the fluid. The host rock Eu content is likely to be controlled by the presence/absence of Ca-plagioclase (40). Accordingly, variations in Eu/Eu* in the vein calcite precipitating from a fluid will be dependent on both the location and degree of fluid-rock reaction, as well as the oxidation state of the fluid.

Higher Ce/Ce* values occur over the same region as $\delta^{13}C$ decreases. Over the same region, the lowest values of Eu/Eu* are measured. Bau and Moller (1992) (30) suggest that the generation of a Ce and Eu anomaly in the same physicochemical environment is impossible (i.e. changing only the fluid oxidation state cannot cause both a negative Eu anomaly and positive Ce anomaly). Thus, we suggest that the covariance in Eu and Ce anomalies observed in this study is caused by enhanced fluid-rock reaction with a Eu-depleted host rock (causing a negative Eu anomaly), coupled with a change in fluid oxidation state (generating a positive Ce anomaly) This generated a fluid with a depleted Eu/Eu*, lower $\delta^{13}C$, and higher Ce/Ce*.

6 Model for Vein Formation

From our textural observations and chemical information collected from this fibrous vein, we suggest that:

(1) Calcite in the vein precipitated from fluid derived externally to the host rocks. This is demonstrated by the depleted $\delta^{18}O$ signature of the vein calcite compared to the surrounding host rocks. Therefore, this fluid was sourced from an external fluid reservoir.
(2) Coarse-scale (several mm) textural zonation in the vein indicates a minimum of four different stages in the growth history of this antitaxial vein.
(3) Asymmetry in the chemical and stable isotope zonation in TZ 4 and 5 on either side of the median line indicate asynchronous, incremental vein growth and different growth rates on either side of the median line.
(4) Each textural zone is characterised by a different suite of trace element, REE and isotopic compositions. We suggest that these changes are due to variations in fluid chemistry during vein growth, most probably caused by variations in fluid-rock reaction along changing flow pathways.

Oliver and Bons (10) predicted that antitaxial fibrous veins would show symmetrical chemical profiles about the median line. Our high spatial-resolution chemical profiles clearly demonstrate asymmetry about the median line. The variations in Sr, C and O isotope ratios, and changes in trace and REE concentrations across the textural zones indicate that different stages of vein growth were accompanied by the influx of fluids that had undergone varying fluid-rock reaction. Changes in the intensity of fluid-rock interaction could be caused by changes in fluid pathways and reactive path lengths (Fig. 7). Alternatively, these changes could be caused by chemical "armouring" of pathways, with fluid chemistry changing as a result of variable fluid velocities and fluid-rock reaction along these pathways. Changes in reactive path lengths can be driven by 'toggle-switch' permeability changes (41), whereby local permeabilities may change over very short periods of time. Such rapid permeability changes could be caused by periodic cycles of vein opening and sealing, related to hydrofracturing and fault rupture during earthquake slip.

The broad scale chemical changes (between different textural zones) are modulated by submillimetre scale fluctuations within textural zones. These fluctuations may be due to crystal growth processes previously discussed, with supersaturation-nucleation-depletion cycles causing varying fractionation of trace and REEs. Alternatively, the high-spatial resolution variations may be caused by changes in the bulk fluid composition, possibly due to multiple pulses of chemically distinct fluid flowing through the vein. If the variations are due to multiple fluid pulses, this could imply that a fine-scale crack-seal process was involved in forming the vein, similar to the mechanism described

by (3).

The formation of a fibrous texture requires extremely limited growth competition between adjacent crystals, so that the growth of grains is not occluded by more rapidly growing neighbours (6). Such limited growth competition may be caused by a very small vein aperture (42). Following the laboratory work of (8), some authors (e.g. 9; 10) have suggested that fibrous veins grow purely by pervasive, grain-scale diffusional processes, without the need for fracture formation. However, we have clearly demonstrated in this study that fibrous veins can form in a fracture-controlled, advective flow regime.

7 Conclusions

Textural observations combined with high-spatial resolution chemical analyses of veins provide a record of changes in fluid chemistry and evidence for changes in fluid flow pathways during vein growth. In this study, high spatial resolution analyses of $\delta^{18}O$, $\delta^{13}C$, $^{87}Sr/^{86}Sr$, minor, trace and rare earth elements were carried out on a fibrous, antitaxial vein. This vein formed during regional mid to late Devonian crustal shortening, at depths of 5-10 km and temperatures of 150–200 °C. The vein formed within a regional-scale, upward fluid flow regime. Low $\delta^{18}O$ fluids were derived from a reservoir external to the host limestone sequence.

The analyses reveal millimetre to submillimetre scale variations in the trace element and isotopic composition of vein calcite, formed during the incremental development of 5 texturally distinct zones within the vein. Adjacent textural zones (TZ 1–4) have different $^{87}Sr/^{86}Sr$ ratios. These changes indicate that the intensity and/or style of fluid-rock reaction changed during the growth of each textural zone. This change in fluid-rock interaction likely reflects changes in fluid flow pathways or the chemistry of fluid reservoirs (Fig. 7).

Textural zones 4 and 5 may have grown broadly contemporaneously on either side of the median line. However, asymmetry in the evolution of $\delta^{18}O$ and $\delta^{13}C$ indicate that vein growth occurred at different rates on either side of the median line. In addition, aspects of the chemical evolution of TZ 4 are not mirrored in TZ 5 (e.g. Fe, Sr, Eu/Eu*). Accordingly, incremental calcite growth events on either side of the median line must have been asynchronous for a substantial part of the growth history of TZs 4 and 5.

Textural zones 1–3 have markedly depleted $\delta^{13}C$ signatures, which are probably the result of the influx of more oxidised fluids in the later stages of vein growth. Cerium and Eu anomalies in calcite veins may provide a record of fluid oxidation state and fluid-rock reaction, and warrant further investiga-

tion, particularly in veins where a growth history may be determined from textural observations.

The association between textural zones and changes in calcite chemistry suggests a coupling between different episodes of vein growth and changes in fluid chemistry. Fluid flow pathways, and the intensity of fluid-rock interaction are interpreted to have varied during vein growth. Our observations and analyses are not consistent with models for antitaxial fibrous vein formation which suggest that vein growth occurs continuously, as a result of pervasive (grain-scale) fluid flow through the surrounding rocks. Furthermore, local scale diffusion of material from the surrounding wall rocks cannot explain the variations in C, O and Sr isotope compositions. Our observations are consistent only with vein growth in a discontinuous flow regime, in which calcite precipitated from fluid which migrated along episodically changing pathways.

8 Acknowledgements

Ken and Sally Kilpatrick are thanked for land access and generous hospitality. Thanks to Joe Cali and Heather Scott-Gagan for providing able technical help with stable isotope mass spectrometry. Les Kinsley kept the Neptune running smoothly. Mike Shelley, Chuck Magee and Charlotte Allen provided help with LA-ICPMS analyses. Chris McFarlane is thanked for helping produce the EMP maps. Harri Kokkonen helped with petrographic preparation. Hugh O'Neill, Ian Campbell, D.C. 'Bear' McPhail, Mike Begbie, Steve Micklethwaite, Silvio Giger and many others provided useful discussions. Nick Oliver and an anonymous reviewer are thanked for their constructive comments. Scott King is thanked for editorial guidance. SLLB is in receipt of an Australian Postgraduate Award, and acknowledges RSES and the ANU for additional scholarship support.

References

[1] W. Buckland, Geology and mineralogy considered with reference to natural theology, William Pickering, London, 1836.

[2] C. Hulin, Structural control of ore deposition, Economic Geology and the Bulletin of the Society of Economic Geologists 24 (1) (1929) 15–49.

[3] J. Ramsay, The crack-seal mechanism of rock deformation, Nature (London) 284 (5752) (1980) 135–139.

[4] S. Cox, M. Etheridge, Crack-seal fibre growth mechanisms and their significance in the development of oriented layer silicate microstructures, Tectonophysics 92 (1983) 147–170.

[5] R. Sibson, A note on fault reactivation, Journal of Structural Geology 7 (6) (1985) 751–754.

[6] S. Cox, Antitaxial crack-seal vein microstructures and their relationship to displacement paths, Journal of Structural Geology 9 (7) (1987) 779–787.

[7] J. Urai, P. Williams, H. van Roermund, Kinematics of crystal growth in syntectonic fibrous veins, Journal of Structural Geology 13 (7) (1991) 823–836.

[8] W. Means, T. Li, A laboratory simulation of fibrous veins: some first observations, Journal of Structural Geology 23 (6-7) (2001) 857–863.

[9] D. Wiltschko, J. Morse, Crystallization pressure versus 'crack seal' as the mechanism for banded veins, Geology 29 (1) (2001) 79–82.

[10] N. Oliver, P. Bons, Mechanisms of fluid flow and fluid-rock interaction in fossil metamorphic hydrothermal systems inferred from vein-wallrock patterns, geometry and microstructure, Geofluids 1 (2) (2001) 137–162.

[11] C. Hilgers, D. Koehn, P. Bons, J. Urai, Development of crystal morphology during unitaxial growth in a progressively widening vein; II. numerical simulations of the evolution of antitaxial fibrous veins, Journal of Structural Geology 23 (2001) 873–885.

[12] P. Bons, The formation of veins and their microstructures, Journal of the Virtual Explorer 2.

[13] D. Durney, J. Ramsay, Incremental strains measured by syntectonic crystal growths, in: Gravity and Tectonics, Wiley, New York, 1973.

[14] M. Etheridge, V. Wall, S. Cox, R. Vernon, High fluid pressures during regional metamorphism and deformation - implications for mass transport and deformation mechanisms, Journal of Geophysical Research, B, Solid Earth and Planets 89 (1984) 4344–4358.

[15] Y. Lee, J. Morse, D. Wiltschko, An experimentally verified model for calcite precipitation in veins, Chemical Geology 130 (3-4) (1996) 203–215.

[16] C. Hilgers, G. Dilg, J. Urai, Microstructural evolution of syntaxial veins formed by advective flow, Geology 32 (3) (2004) 261–264.

[17] I. Browne, Stratigraphy and structure of the Devonian rocks of the Taemas and Cavan areas, Murrumbidgee River, south of Yass, N.S.W, Jour-

nal and Proceedings of the Royal Society of New South Wales 4 (1958) 115–128.

[18] J. Cramsie, D. Pogson, C. Baker, Yass 1:100,000 geological sheet 8628 (1975).

[19] R. Glen, Thrust, extensional and strike-slip tectonics in an evolving Palaeozoic orogen; a structural synthesis of the Lachlan Orogen of south-eastern Australia, Tectonophysics 214; 1-4 (1992) 341–380.

[20] S. Eggins, L. Kinsley, J. Shelley, Deposition and element fractionation processes during atmospheric pressure laser sampling for analysis by ICP-MS, Applied Surface Science 127-129 (1998) 278–286.

[21] H. Longerich, S. Jackson, D. Gunter, Laser ablation inductively coupled plasma mass spectrometric transient signal data acquisition and analyte concentration calculation, Journal of Analytical Atomic Spectrometry 11 (1996) 899–904.

[22] S. Eggins, R. Grun, M. T. McCulloch, A. W. Pike, J. Chappell, L. Kinsley, G. Mortimer, M. Shelley, C. V. Murray-Wallace, C. Spotl, L. Taylor, In situ U-series dating by laser-ablation multi-collector ICPMS: new prospects for Quaternary geochronology, Quaternary Science Reviews 24 (2005) 2523–2538.

[23] F. C. Ramos, J. A. Wolff, D. L. Tollstrup, Measuring $^{87}Sr/^{87}Sr$ variations in minerals and groundmass from basalts using LA-MC-ICPMS, Chemical Geology 211 (2004) 135–158.

[24] J. Woodhead, S. Swearer, J. Hergt, R. Maas, In situ Sr-isotope analysis of carbonates by LA-MC-ICP-MS: interference corrections, high spatial resolution and an example from otolith studies, Journal of Analytical Atomic Spectrometry 20 (2005) 22–27.

[25] M. Gagan, A. Chivas, P. Isdale, High-resolution isotopic records from corals using ocean temperature and mass-spawning chronometers, Earth and Planetary Science Letters 121 (3-4) (1994) 549–558.

[26] T. Coplen, C. Kendall, J. Hopple, Comparison of stable isotope reference samples, Nature 302 (1983) 236–239.

[27] E. Dromgoole, L. Walter, Iron and manganese incorporation into calcite; effects of growth kinetics, temperature and solution chemistry, Chemical Geology 81 (4) (1990) 311–336.

[28] E. Watson, A conceptual model for near-surface kinetic controls on the trace-element and stable isotope composition of abiogenic calcite crystals, Geochimica et Cosmochimica Acta 68 (7) (2004) 1473–1488.

[29] S. Lee, D. Lee, Y. Kim, B. Chae, W. Kim, N. Woo, Rare earth elements as indicators of groundwater environment changes in a fractured rock system; evidence from fracture-filling calcite, Applied Geochemistry 18 (1) (2003) 135–143.

[30] M. Bau, P. Moller, Rare earth element fractionation in metamorphogenic hydrothermal calcite, magnesite and siderite, Mineralogy and Petrology 45 (1992) 231–246.

[31] D. Towell, J. Winchester, R. Spirn, Rare-earth distributions in some rocks

and associated minerals of the batholith of southern California, Journal of Geophysical Research 70 (1965) 3485–3496.
[32] W. McDonough, S.-s. Sun, The composition of the earth, Chemical Geology 120 (3-4) (1995) 223–253.
[33] G. Faure, J. Powell, Strontium isotope geology, Springer, New York, 1972.
[34] R. Denison, R. Koepnick, W. Burke, E. Hetherington, A. Fletcher, Construction of the Silurian and Devonian seawater $^{87}sr/^{86}sr$ curve, Chemical Geology 140 (1-2) (1997) 109–121.
[35] M. Elburg, P. Bons, J. Foden, C. Passchier, The origin of fibrous veins: constraints from geochemistry, in: S. De Meer, M. Drury, J. De Bresser, G. Pennock (Eds.), Deformation mechanisms, rheology and tectonics: Current status and future perspectives, Vol. 200, Geological Society Special publications, London, 2002, pp. 103–118.
[36] S.-T. Kim, J. O'Neil, Equilibrium and nonequilibrium oxygen isotope effects in synthetic carbonates, Geochimica et Cosmochimica Acta 61 (1997) 3461–3475.
[37] P. Deines, D. Langmuir, R. Harmon, Stable carbon isotope ratios and the existence of a gas phase in the evolution of carbonate ground waters, Geochimica et Cosmochimica Acta 38 (1974) 1147–1164.
[38] P. Ortoleva, E. Merino, C. Moore, J. Chadam, Geochemical self-organization I; reaction-transport feedbacks and modeling approach, American Journal of Science 287 (10) (1987) 979–1007.
[39] H. Ohmoto, M. Goldhaber, Geochemistry of Hydrothermal Ore Deposits, 3rd Edition, John Wiley and Sons, New York, 1997, Ch. Sulfur and Carbon Isotopes, pp. 517–611.
[40] C. C. Schnetzler, J. A. Philpotts, Partition coefficients of rare-earth elements between igneous matrix material and rock-forming mineral phenocrysts - II, Geochimica et Cosmochimica Acta 34 (1970) 331–340.
[41] S. Miller, A. Nur, Permeability as a toggle switch in fluid-controlled crustal processes, Earth and Planetary Science Letters 83 (2000) 133–146.
[42] C. Hilgers, J. Urai, Microstructural observations on natural syntectonic fibrous veins; implications for the growth process, Tectonophysics 352 (3-4) (2002) 257–274.

References

9 Figure Captions

Figure 1: Summary of textural zones in antitaxial vein calcite from the Murrumbidgee Group, New South Wales, Australia. (a) Polished thick section. The median line (dotted) and five textural zones (TZ, dashed) are described in the text. Arrow indicates barite fibre within calcite. Note that wall rock on the lower side of the vein was removed during sample preparation. The red box indicates the approximate area in which Sr isotopes and trace elements were analysed by laser ablation (LA-ICP-MS). Carbon and oxygen isotopes were analysed along a sampling transect located immediately to the right of this box. (b) Polished thin section from sample area shown in (a). The boundaries between textural zones TZ1, TZ2 and TZ3 have not been marked to enable them to be seen more easily. (c) Cathodoluminesence photomicrograph of area 'c' shown in (b). Different textural zones have different luminescence. Note micron-scale and spatial precision of laser ablation analyses (LA-ICP-MS), which enable different textural zones to be individually sampled.

Figure 2: Summary of LA-ICP-MS sampling protocol for $^{87}Sr/^{86}Sr$ and trace element analyses. (a) Area of vein over which trace elements and $^{87}Sr/^{86}Sr$ were analysed with interpretative sketch. Holes (shown by black dots on sketch) mark the locations of individual $^{87}Sr/^{86}Sr$ analyses. (b) Results of spot analyses (black squares) for $^{87}Sr/^{86}Sr$. Error bars on spot analyses are 2 standard errors. Note significant differences in $^{87}Sr/^{86}Sr$ (at 95% confidence level) between TZ2, TZ3 and TZ4.

Figure 3: Calcite $\delta^{13}C$ (relative to VPDB) and $\delta^{18}O$ (relative to VSMOW) as a function of distance from the median line of the vein. Spatial resolution is 100 μm. Note asymmetry of $\delta^{18}O$ about the median line, and significantly lower $\delta^{13}C$ values in TZ 1-3.

Figure 4: (a) Electron microprobe maps of iron, magnesium and strontium across the vein. Accompanying 150 μm moving average LA-ICP-MS profiles are shown for Fe, Mg and Sr (traverse 1 is solid black, traverse 2 is dashed). Note that LA-ICP-MS profiles are separated by approximately 5 mm along the vein, and cross several different fibres. Fine-scale (< 1 mm) heterogeneity of trace element concentrations are apparent, while broader trends correlate with the different textural zones. Point 'α' refers to an crosscutting, apparently late, high Sr region. Values for other trace elements are listed in the supplementary data sets. (b) Comparison of traverse 1 (grey) with profile along a single fibre (150 μm moving average). Note broad-scale agreement between profiles, with significant fine-scale variation.

Figure 5: Cerium (Ce/Ce*) and europium (Eu/Eu*) anomalies as a function of distance from the median line of the vein (determined from LA-ICP-MS

analyses, 150 μm moving average). The δ^{13}C profile (from Fig. 3) has been replotted for comparison with the LA-ICP-MS analyses. Note the relatively high Ce/Ce* ratios, low Eu/Eu* ratios, and low δ^{13}C values in TZ 1-3.

Figure 6: (a) Schematic diagram (after Bau and Moller, 1992; 30) showing REE patterns in calcite expected for CO_3^{2-} poor and rich solutions (b) Plot of slope of chondrite normalised REE (see text for explanation) as a function of distance from the median line (150 μm moving average). Note high-frequency oscillations and enrichment in heavy rare earth elements (HREEs) in TZ 1-3.

Figure 7: Schematic interpretation of fluid migration in a fault-fracture network, as recorded by the chemistry of antitaxial vein calcite. (a) Fluid migration along hypothetical flow pathways (1, 2) in a fault-fracture network. Externally sourced fluids migrating along different flow pathways lead to distinct variations in fluid chemistry. (b) Photomicrograph of fibrous antitaxial vein with summary of the variation in δ^{18}O values in different textural zones.

10 Tables

Table 1

Finnigan Neptune collector configuration employed for LA-ICPMS analysis.

Faraday	L4	L3	L2	L1	C	H1	H2	H3	H4
Isotope	^{83}Kr	^{167}Er^{++}	^{84}Sr	^{85}Rb	^{86}Sr	^{173}Yb^{++}	^{87}Sr	^{88}Sr	^{177}Hf^{++}
Actual mass	82.914	83.465	83.933	84.912	85.929	86.469	86.929	87.926	88.471

Table 2

Average $^{87}Sr/^{86}Sr$ and 2 σ errors for each textural zone determined from the spot analyses.

Analysis	Textural Zone	Average $^{87}Sr/^{86}Sr$	±2 s.e.
Spot (TS20-01)	2	0.70828	0.00002
Spot (TS20-02)	2	0.70831	0.00006
Spot (TS20-02)	3	0.70812	0.00003
Spot (TS20-04)	3	0.70815	0.00003
Spot (TS20-05)	3	0.70817	0.00003
Spot (TS20-06)	4	0.70825	0.00002
Spot (TS20-07)	4	0.70823	0.00003
Spot (TS20-08)	4	0.70822	0.00003
Spot (TS20-09)	4	0.70820	0.00004
Spot (TS20-10)	4	0.70822	0.00003
Spot (TS20-11)	4	0.70823	0.00003
Spot (TS20-12)	4	0.70823	0.00003
Spot (TS20-13)	5	0.70824	0.00004
Spot (TS20-14)	5	0.70822	0.00004
Spot (TS20-15)	5	0.70827	0.00004
Spot (TS20-16)	5	0.70825	0.00003
Spot (TS20-17)	5	0.70824	0.00004
Spot (TS20-18)	5	0.70822	0.00003

11 Figures

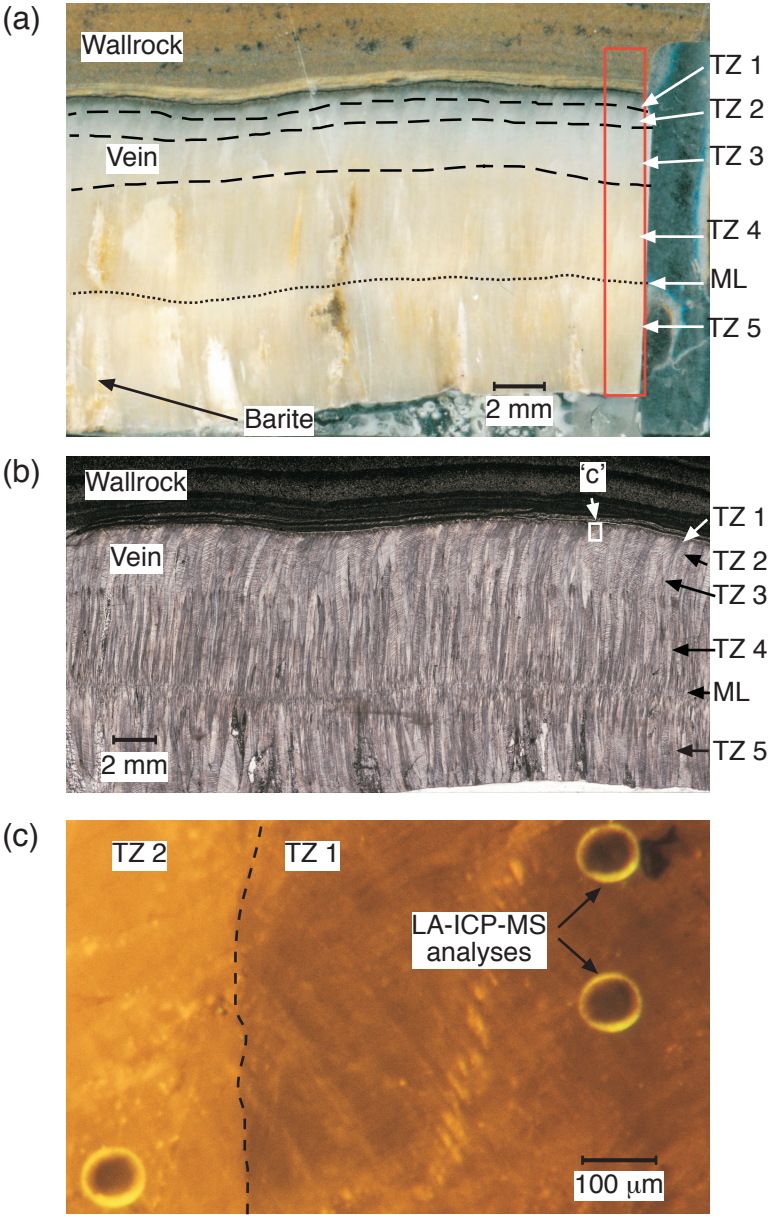
(a)
Wallrock
Vein
Barite
2 mm
TZ 1
TZ 2
TZ 3
TZ 4
ML
TZ 5
(b)
Wallrock
'c'
Vein
2 mm
TZ 1
TZ 2
TZ 3
TZ 4
ML
TZ 5
(c)
TZ 2
TZ 1
LA-ICP-MS
analyses
100 μm